# Gravitational-wave imprints of nonconvex dynamics in binary neutron star mergers

Giuseppe Rivieccio,[1] Davide Guerra,[1] Milton Ruiz,[1] and José A. Font[1,2]

[1]*Departament d'Astronomia i Astrofísica, Universitat de València, C/ Dr Moliner 50, 46100 Burjassot, Valencia, Spain*

[2]*Observatori Astronòmic, Universitat de València, C/ Catedrático José Beltrán 2, 46980 Paterna, Valencia, Spain*

(Received 18 January 2024; accepted 26 February 2024; published 13 March 2024)

Explaining gravitational-wave (GW) observations of binary neutron star (BNS) mergers requires an understanding of matter beyond nuclear saturation density. Our current knowledge of the properties of high-density matter relies on electromagnetic and GW observations, nuclear physics experiments, and general relativistic numerical simulations. In this paper we perform numerical-relativity simulations of BNS mergers subject to nonconvex dynamics, allowing for the appearance of expansive shock waves and compressive rarefactions. Using a phenomenological nonconvex equation of state we identify observable imprints on the GW spectra of the remnant. In particular, we find that nonconvexity induces a significant shift in the quasiuniversal relation between the peak frequency of the dominant mode and the tidal deformability (of order $\Delta f_{\rm peak} \gtrsim 380$ Hz) with respect to that of binaries with convex (regular) dynamics. Similar shifts have been reported in the literature, attributed however to first-order phase transitions from nuclear/hadronic matter to deconfined quark matter. We argue that the ultimate origin of the frequency shifts is to be found in the presence of anomalous, nonconvex dynamics in the binary remnant.

DOI: 10.1103/PhysRevD.109.064032

## I. INTRODUCTION

Gravitational waves (GWs) from binary neutron star (BNS) mergers encode key information about the nature of matter above nuclear saturation density ($n_0 = 0.15 \pm 0.01$ fm$^{-3}$). Following merger, the bulk of the GW energy is emitted and reaches values of $\sim 0.1 M_\odot c^2$ [1]. This energy is emitted at frequencies $\gtrsim 2$ kHz and would be observable with the third-generation detectors Einstein Telescope and Cosmic Explorer [2–4]. The GW spectrum is directly linked to properties of NS [5] and can be used to impose tight constraints on the equation of state (EOS), complementary to those from electromagnetic (EM) observations and heavy-ion experiments [6–8]. These constraints can in turn be used to infer a number of key properties of a NS, as e.g., the mass-radius relationship, the tidal deformability, or the moment of inertia. In particular, numerical work has shown that the GW spectra of the remnant is characterized by the presence of distinctive peaks associated with different oscillation modes (see e.g., [9,10] and references therein). The frequencies of various such modes, e.g., the peak frequency at merger $f_{\rm peak}$ and the quadrupolar mode frequency $f_2$, have been found to be related quasiuniversally with the tidal deformability parameter $\Lambda$ characterising the quadrupolar deformability of an isolated NS.

Numerical relativity simulations of BNS mergers have also revealed that following merger the temperature inside the densest parts of the binary remnant remains below $T \lesssim 10$ MeV, while hot patches of matter with $T \gtrsim 50$ MeV eventually appear, triggering the formation of a hot annulus (see e.g., [11–14]). Through angular momentum transport, matter in the outer region of the system gains enough rotational energy to be ejected, while the inner part contracts to form a central core, which may undergo a transition to quark-gluon plasma or other exotic states [15–17]. It has also been shown (see e.g., [18–20]) that particle production such as hyperons, a process that becomes relevant as the temperature increases, can trigger a substantial drop in the thermal pressure of the binary remnant.

Although there have been considerable efforts into the theoretical understanding of the EOS beyond nuclear saturation density, systematic calculations of matter properties at densities larger than $n_0$ based on quantum chromodynamics (QCD) are still not possible. Therefore, many properties of phase transitions remain unclear, e.g., the threshold temperature or the densities at which the system undergoes a phase transition are unknown [21]. So far, QCD calculations assuming a vanishing baryonic chemical potential $\mu$ predict that a smooth crossover transition will take place at a temperature of $T = 154 \pm 9$ MeV [22–24]. Unfortunately, at $\mu \neq 0$ only perturbative calculation or phenomenological QCD models exist [25–27], and they are not, in particular, applicable in regions of first-order phase transitions.

 

The possible appearance of phase transitions from nuclear hadronic matter into quark-gluon plasma or into matter phases containing exotic particles (e.g., hyperons) in BNS mergers may modify the stability, dynamics and final fate of the remnant, and thus the associated GW signal. Numerical studies have sought to identify the imprints of the first-order hadron-quark phase transition on the GWs (see e.g., [16,21,28–31]). In particular, the BNS merger simulations of [21,29] showed that if the remnant undergoes a strong first-order phase transition to deconfined quarks, the dominant GW frequency at merger $f_{\rm peak}$ exhibits a significant deviation from a quasiuniversal (i.e., EOS-insensitive) relation with the tidal deformability $\Lambda$, an effect that could be observationally identified. We note that phase transitions soften[1] the EOS at merger, which potentially can modify the ejecta properties and, hence, any EM counterpart [16,28,29,32].

Physical processes involving high-density matter where the system undergoes a phase transition to exotic states also affect the monotonic increase of the speed of sound with density. In particular, at densities above $n_0$ monotonicity is lost [22–24,33–39]. The nonmonotonicity of the sound speed can also result from the behavior of the adiabatic index at such densities [40]. The speed of sound is closely related to the so-called convexity of the EOS. Namely, the convexity of a thermodynamical system is determined by the sign of the so-called fundamental derivative $\mathcal{G}$ on the $p$–$V$ plane [41,42], a quantity directly connected to the derivative of the speed of sound. Here $p$ and $V = \rho_0^{-1}$ are the pressure and the specific volume, respectively, with $\rho_0$ the rest-mass density. When $\mathcal{G} > 0$ isentropes on the $p$–$V$ plane are convex and the dynamics of the system involves compressive shocks and expansive rarefaction waves [43]. Such physical systems are said to be convex. By contrast, when $\mathcal{G} < 0$ the dynamics becomes "anomalous," involving expansive shocks and compressive rarefaction waves, and the system is said to be nonconvex.

In the presence of phase transitions to exotic components, the fundamental derivative can indeed be negative, implying that the EOS should be nonconvex in that regime. This would lead to nonconvex, atypical dynamics. In particular, at the phase transition the fundamental derivative is discontinuous, i.e., in the continuous limit there is a single point along an isentrope where $\mathcal{G} < 0$. However, state-of-the-art numerical simulations of BNS mergers employ microphysical, finite-temperature EOS tables constructed using data from observations and nuclear physics [44–46]. Because of the discrete nature of the tables, it is unlikely that tabulated points coincided with the locus of the discontinuity of the fundamental derivative which may cause nonconvex behavior to spread spuriously along neighboring points. Besides, finite difference derivatives of the thermodynamical variables may also induce spurious oscillations in $\mathcal{G}$, artificially triggering nonconvex dynamics in a finite region. An example of numerical loss of convexity associated with insufficient thermodynamic discretization of some tabulated EOSs when the adiabatic index is nonconstant was reported in [47].

Studies of nonconvex, relativistic fluid dynamics and magnetohydrodynamics (MHD) have been presented in [48–54]. Particularly relevant for the topic discussed in this paper are the results reported in [50,51,53]. In particular [51] probed the effects of a nonconvex EOS on the dynamics of both spherically symmetric and uniformly rotating NS undergoing gravitational collapse to black holes (BHs). The stars were evolved assuming a phenomenological $\Gamma$-law EOS first proposed in [50] for which the adiabatic index $\Gamma$ depends on the rest-mass density in a way which leads to $\mathcal{G} < 0$ in some regions of the rest-mass density distribution. The results of [51] showed that a nonconvex EOS has a major effect on the dynamics of gravitational collapse, accelerating the onset of the collapse and leaving distinctive imprints on the GW signal, as compared to the case of a convex dynamics. Moreover, [51] suggested that to properly capture the transition from nuclear matter to exotic matter states, EOS tables should be more densely populated with nodal points along regions where the fundamental derivative displays large variations, specially when these variations drive negative values of $\mathcal{G}$. We also note that [51] pointed out that convexity across phase transitions may occasionally be recovered numerically if the singularities in the Gibbs or Helmholtz free energies are removable. Thermodynamic consistency requires the Gibbs free energy to be a jointly concave function. This requirement can be imposed by convolving the Gibbs free energy with a non-negative smoothing function, which smoothes out singularities along phase transitions [41]. Recently, an analytic model for a tabulated EOS that focuses on the modeling of phase transitions through a thermodynamically adaptive piecewise-polytropic approximation has been reported [53]. This method is able to reproduce the nonconvex behavior of several nuclear EOSs.

In this work we analyze the possible repercussion the use of a nonconvex EOS may have on the dynamics of BNS mergers, focusing in particular on the evolution of the postmerger remnant. These astrophysical systems offer a perfect framework to study the impact of nonconvex thermodynamics on their (hydro)dynamics, as they are characterized by the presence of high-density regions (above nuclear saturation density) where the dynamics may become nonconvex. Moreover, they also allow to investigate the potential influence of nonconvex effects on multimessenger observables such as GW and EM waves. Here, we perform a numerical-relativity survey of BNS

[1]In a NS modeled with a stiff (soft) EOS the pressure increases promptly with density. Hence, its core is relatively resistant (susceptible) to compression giving rise to stars with larger (smaller) radii.

mergers in quasicircular orbit that merge and form a transient remnant. The stars are assumed to be irrotational and are modeled using piecewise-polytropic representations of different microphysical, nuclear EOSs. The effects of nonconvex thermodynamics in the BNS mergers are incorporated using the same phenomenological EOS employed in [50,51], i.e., a Γ-law EOS allowing for shock heating. Following [50] we assume that the adiabatic index Γ is not constant but depends on the rest-mass density. This allows us to mimic some key features of tabulated, nuclear-matter EOS such as the nonmonotonic dependence of the speed of sound (or the adiabatic index) with the rest-mass density [55] and, thus, the appearance of nonconvex dynamics. We find that the use of a nonconvex EOS does influence the postmerger dynamics in a significant way. In particular, nonconvex dynamics can strongly impact the frequency of the peak first visible in the GW spectra right after merger, $f_{\rm peak}$. Depending on the parameters of our EOS, deviations from a $\Lambda - f_{\rm peak}$ quasiuniversal relation can be in magnitude as large as $\Delta f_{\rm peak} \geq 380$ Hz with respect to that of binaries with pure convex evolution. Such frequency shifts are reminiscent of the results reported by [21,29], where they were attributed as due to a strong first-order phase transitions from nuclear/hadronic matter to deconfined quark matter. We argue that the explanation for the observed frequency shift is to be found in the presence of anomalous, nonconvex dynamics in the binary remnant. Our explanation does not exclude the interpretation of the shifts as due to a first-order phase transition, as the dynamics is indeed nonconvex there. The explanation based on the existence of a first-order phase transition can be regarded as a particular manifestation of a more general reason, namely the possible nonmonotonic behavior of the EOS of NSs above nuclear saturation density.

The rest of the paper is organized as follows: Sec. II presents a brief summary of non-convex thermodynamics and of the phenomenological EOS used in this study. The description of the numerical methods employed in the simulations of BNS mergers, including also the initial data and the grid structure, are given in Secs. III A and III B. We present our results in Sec. IV and summarize our findings and conclusions in Sec. V. Finally, the Appendix gathers further evidence from additional simulations to validate our main findings.

## II. NONCONVEX THERMODYNAMICS AND EOS

The study of the physical properties of BNS merger remnants requires of the understanding of the EOS at densities typically higher than nuclear saturation density. As discussed above, at such densities the system may develop nonconvex dynamics. In the following, we summarize key properties of nonconvex dynamics, referring the reader to [50,51] for further details.

The convexity properties of Newtonian hydrodynamical flows is determined by the EOS through the concept of the fundamental derivative [43,56,57] defined as

$$\mathcal{G} \equiv -\frac{1}{2} V \frac{\frac{\partial^2 p}{\partial V^2}\big|_s}{\frac{\partial p}{\partial V}\big|_s}, \tag{1}$$

with $s$ being the specific entropy. A change in the sign of the fundamental derivative measures the convexity of the isentropes on the $p$–$V$ plane. When $\mathcal{G} > 0$ the system is convex and its dynamics involves expansive rarefaction waves and compressive shocks. This is the usual regime in which many astrophysical scenarios develop. By contrast, when $\mathcal{G} < 0$ the system is nonconvex and its (anomalous) dynamics involves compressive rarefaction waves and expansive shocks. This nonstandard behavior has been experimentally observed in transonic and mildly supersonic fluids [58,59]. Fluids attaining negative values of the fundamental derivative are called Bethe-Zel'dovich–Thompson fluids, after [43,56,57].

Following [41,50], the speed of sound $c_s$ can be related to the fundamental derivative as

$$\mathcal{G} = 1 + \frac{\partial \ln c_s}{\partial \ln \rho_0}\bigg|_s. \tag{2}$$

Therefore, the fundamental derivative becomes negative when $\partial \ln c_s / \partial \ln \rho_0|_s < -1$. A generalized fundamental derivative for relativistic fluids was found in [48], given by

$$\mathcal{G}_R = \mathcal{G} - \frac{3}{2} c^2_{s(R)}, \tag{3}$$

where $c_{s(R)}$ is the relativistic speed of sound that can be related to $c_s$ through $c_s^2 = h c^2_{s(R)}$ where $h = 1 + \epsilon + p/\rho_0$ is the specific enthalpy and $\epsilon$ is the specific internal energy density.

Figure 1 displays the relativistic fundamental derivative for a set of selected EOSs from the CompOSE database [60] as a function of baryon density $n_b$. EOS DD2F-SF and EOS DD2-SF include a phase transition to hadron-quark matter while EOS DD2 does not. The presence of the phase transition induces the loss of monotonicity of the speed of sound which, subsequently, triggers the loss of convexity. Indeed, at densities where the EOS suffers a phase transition, the relativistic fundamental derivative $\mathcal{G}_R$ (as well as the Newtonian one) becomes negative. Notice that, as pointed out in [51], the oscillating behavior in $\mathcal{G}_R$ is a numerical artifact due to the computation of the fundamental derivative using a discrete EOS table. This causes the nonconvex behavior to spread spuriously along neighboring points.

Using the above definitions, the effects of a nonconvex EOS on the stability and dynamics of isolated NS were probed in [51] employing a phenomenological Gaussian

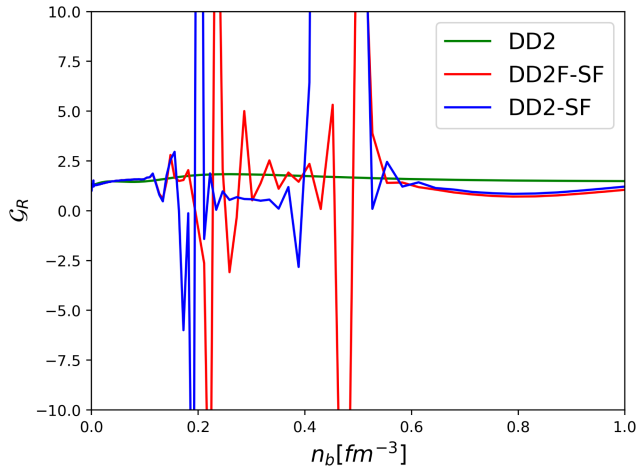


FIG. 1. Relativistic fundamental derivative $\mathcal{G}_R$ as a function of baryon density $n_b$ for a few selected EOS with (DD2F-SF and DD2-SF) and without (DD2) a first-order hadron-quark phase transition.

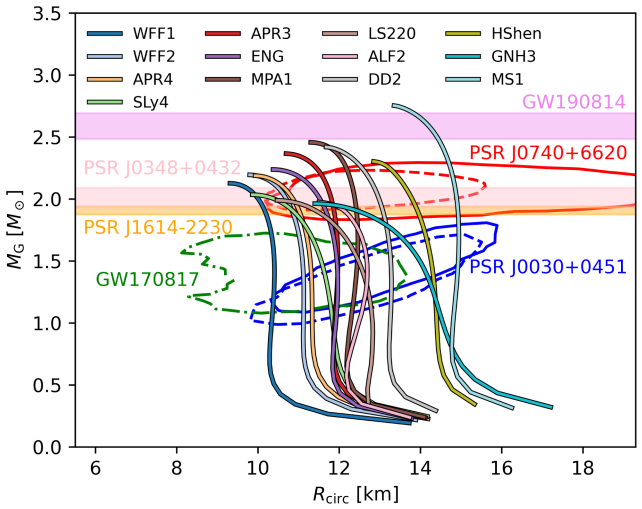


FIG. 2. Gravitational mass $M_G$ vs circumferential radius $R_{\rm circ}$ for all the EOSs listed in Table I along with the observational NS mass constraints within 95% confidence levels from the measurements of pulsars from NICER/XMM-Newton [65,66,71], and the BNS observations from the LIGO/Virgo/KAGRA Collaboration [70,72].

$\Gamma$-law (GGL) EOS $p = (\Gamma - 1)\rho_0\epsilon$. Here $\Gamma$ is an effective thermal index that, to mimic its dependency on the nucleon effective mass for densities above half nuclear saturation [55], is given by [50]

$$\Gamma = \Gamma_{\rm th} + (\Gamma_1 - \Gamma_{\rm th}) \exp\left[-\frac{(\rho_0 - \rho_1)^2}{\Sigma^2}\right], \qquad (4)$$

where $\Gamma_{\rm th}$, $\Gamma_1$, $\rho_1$, and $\Sigma$ are free constant parameters. The results reported by [51] indicate that a nonconvex dynamics can accelerate the onset of the collapse of the NS to a BH with respect to that of a convex dynamics. Nonconvexity also leaves an imprint on the GW signal, amplifying the amplitude of the GWs emitted by the collapsing star. The maximum amplitude is about twice as large as in the convex case. These imprints are large enough to be detectable by third-generation, ground-based detectors.

## III. NUMERICAL SETUP FOR NONCONVEX BNS MERGER SIMULATIONS

### A. Initial data

We consider BNS configurations in quasiequilibrium circular orbits that inspiral, merge and form dynamical stable remnants lasting more than $\gtrsim$15 ms. The binaries consist of two identical irrotational NS modeled by a piecewise polytropic representation of (several) nuclear EOSs using seven pieces as in [61]. The initial data are computed using the LORENE code [62–64]. The initial coordinate separation of the binary is ∼44.3 km, and the rest mass of each NS is $M_0 = 1.4M_\odot$. The initial properties of our binaries are summarized in Table I. These representative EOSs broadly satisfy the current observational constraints on NS masses and radii (see Fig. 2). For instance, all EOSs predict that the maximum (gravitational) mass configuration of an isolated spherical star is larger than $2M_\odot$, consistent with: (i) $M^{\rm max}_{\rm sph} > 2.072^{+0.067}_{-0.066}M_\odot$ from the NICER and XMM analysis of PSR J0740 + 6620 [65]; (ii) $M^{\rm max}_{\rm sph} > 2.01^{+0.017}_{-0.017}M_\odot$ from the NANOGrav analysis of PSR J1614-2230 [66]; (iii) $M^{\rm max}_{\rm sph} > 2.01^{+0.14}_{-0.14}M_\odot$ from the pulsar timing analysis of PSR J0348 + 0432 [67]; and (iv) $M^{\rm max}_{\rm sph} > 2.14^{+0.20}_{-0.18}M_\odot$ from the NANOGrav and the Green Bank Telescope [68]. However, the LIGO/Virgo/KAGRA analysis of GW170817 predicts that the tidal deformability of a $1.4M_\odot$ NS is $\Lambda_{1.4} = 190^{+390}_{-120}$ at the 90% credible level [69], and hence only a few EOSs in Table I satisfy this constraint. Also note that the constraints imposed by GW190814 are more uncertain as there is not complete confirmation that the secondary of this compact binary coalescence is actually a NS [70]. We stress that we consider these EOSs because, as shown in Fig. 2, they span a large range of NS central rest-mass densities, radii and maximum gravitational masses for irrotational NSs, allowing us to probe the impact of a nonconvex dynamics on the GW spectrum of BNS mergers.

### B. Simulations

Much of the numerical approach employed here has been extensively discussed in previous work (see e.g., [73,74]). Therefore, in the following we only summarize the basic aspects, referring the reader to those references for further details and code tests.

#### 1. Evolution

We carry out the simulations employing the well-tested, publicly available IllinoisGRMHD code [73,74] embedded in

TABLE I. Summary of the initial properties of the BNS configurations. We list the EOS, the gravitational mass $M[M_\odot]$, the compactness $\mathcal{C} \equiv M/R_{\rm eq}$ and the tidal deformability $\Lambda = (2/3)\kappa_2 \mathcal{C}^{-5}$ for each individual star. Here $R_{\rm eq}$ is the equatorial coordinate radius, and $\kappa_2$ is the second Love number. The ADM mass $M_{\rm ADM}[M_\odot]$, the ADM angular momentum $J_{\rm ADM}[M_\odot^2]$, the angular velocity $\Omega$ [krad/s], for an initial binary coordinate separation of ∼44.3 km, and the initial maximum value of the rest-mass of the system $\rho_{0,\rm max}$ [g cm$^{-3}$]. In all cases the NS has a rest-mass $M_0 = 1.4 M_\odot$.

| EOS | $M$ | $\mathcal{C}$ | $\Lambda$ | $M_{\rm ADM}$ | $J_{\rm ADM}$ | $\Omega$ | $\rho_{0,\rm max}$ |
|---|---|---|---|---|---|---|---|
| WFF1 | 1.26 | 0.18 | 406.07 | 2.50 | 6.45 | 1.76 | $10^{15.01}$ |
| WFF2 | 1.27 | 0.17 | 1115.06 | 2.52 | 6.54 | 1.76 | $10^{14.90}$ |
| APR4 | 1.28 | 0.17 | 440.75 | 2.52 | 6.56 | 1.77 | $10^{14.93}$ |
| SLy4 | 1.28 | 0.16 | 511.70 | 2.54 | 6.62 | 1.77 | $10^{14.93}$ |
| APR3 | 1.28 | 0.16 | 620.00 | 2.53 | 6.61 | 1.77 | $10^{14.86}$ |
| ENG | 1.28 | 0.16 | 636.35 | 2.53 | 6.60 | 1.77 | $10^{14.87}$ |
| MPA1 | 1.28 | 0.15 | 784.52 | 2.54 | 6.64 | 1.77 | $10^{14.81}$ |
| LS220 | 1.29 | 0.15 | 899.05 | 2.55 | 6.69 | 1.77 | $10^{14.84}$ |
| ALF2 | 1.29 | 0.15 | 941.42 | 2.54 | 6.66 | 1.77 | $10^{14.79}$ |
| DD2 | 1.29 | 0.13 | 1113.92 | 2.56 | 6.73 | 1.78 | $10^{14.76}$ |
| HShen | 1.30 | 0.14 | 1633.24 | 2.58 | 6.82 | 1.78 | $10^{14.69}$ |
| GNH3 | 1.30 | 0.13 | 1371.15 | 2.58 | 6.81 | 1.78 | $10^{14.77}$ |
| MS1 | 1.30 | 0.13 | 2020.75 | 2.58 | 6.83 | 1.79 | $10^{14.63}$ |

the Einstein Toolkit infrastructure [75], employing the Carpet code [76] for the moving-box mesh capability. The code evolves the Baumgarte-Shapiro-Shibata-Nakamura (BSSN) equations for the spacetime fields [77,78] coupled with puncture gauge conditions cast in first-order form. We use fourth-order spatial stencils. We set the damping coefficient appearing in the shift condition to $1/M_{\rm ADM}$. Fifth-order Kreiss-Oliger dissipation [79] is also added in the BSSN evolution equations. The IllinoisGRMHD code evolves the matter fields using the equations of ideal, general-relativistic MHD, which are cast in a conservative scheme using the Valencia formulation [80–82], via a high-resolution shock-capturing (HRSC) technique [74] that employs the piecewise parabolic method (PPM) [83] coupled to the Harten, Lax, and van Leer (HLL) approximate Riemann solver [84]. The time integration is performed via the method of lines using a fourth-order accurate, Runge-Kutta integration scheme with a Courant-Friedrichs-Lewy factor of 0.45.

We notice that, if the approximate Riemann solver for the system of hydrodynamics equations closed with a nonconvex EOS induces enough numerical viscosity to allow the formation of compound waves, then the resulting numerical scheme is stable (see e.g., [85–87]). In particular, the use of the HLL solver allows us to resolve compound waves [50].

### 2. Grid structure

In all simulations we use three sets of nested refinement boxes centered on each star and on the center of mass of the binary. Each of them contains six boxes that differ in size and in resolution by factors of two. When two boxes overlap they are replaced by a common box centered on the center-of-mass of the BNS. The finest box around the NS has a half-side length of $1.25 R_{\rm NS}$, where $R_{\rm NS}$ is the radius of the NS. The finest level has a resolution of ∼220 m and resolves the star by ∼45 grid point across its radius. We place the outer boundary at ∼1600 km.

### 3. EOS for the dynamical evolution

The cold EOSs listed in Table I are adequate to model the NS prior to merger. However, during merger considerable shock heating increases the internal energy and temperature to values over 10 MeV. Such high temperatures provide additional pressure support that may alter the structure and evolution of the remnant. To account for this and following common practice, we adopt an EOS that has both a thermal and a cold contribution. The total pressure can be expressed as

$$p = p_{\rm th} + p_{\rm cold}, \tag{5}$$

where $p_{\rm cold} = \kappa_i \rho_0^{\Gamma_i}$, with $\kappa_i$ and $\Gamma_i$ the corresponding polytropic constant and the polytropic exponent in the rest-mass density range $\rho_{0,i-1} \le \rho_0 \le \rho_{0,i}$, respectively (see e.g., [61]), and the thermal pressure is given by

$$p_{\rm th} = (\Gamma - 1)\rho_0(\epsilon - \epsilon_{\rm cold}), \tag{6}$$

where

$$\epsilon_{\rm cold} = -\int p_{\rm cold} d(1/\rho_0). \tag{7}$$

Following [50,51], in order to incorporate nonconvex thermodynamics in the evolution of the BNS initial data we employ the phenomenological GGL EOS. Therefore, the effective thermal index $\Gamma$ given by Eq. (4) is used in the thermal part of the pressure, Eq. (6). For comparison purposes with our previous simulations in [88] we set $\Gamma_{\rm th} = 1.8$. The other three parameters of the GGL EOS are chosen such as the resulting EOS is causal, i.e., the speed of sound $c_{s(R)} < 1$. In particular, we set $\rho_1 = 9.1 \times 10^{14}$ g cm$^{-3}$, and $\Sigma = 0.35\,\rho_1$. On the other hand, we consider different values of $\Gamma_1$ to study the impact of this parameter on the EOS and ultimately on the fate of the remnant. In our fiducial model we set $\Gamma_1 = 3.0$ and in some selected cases we set $\Gamma_1 = 3.5$.

Figure 3 displays the convexity behavior of the GGL EOS on the $p - \rho_0$ plane. For typical values of the rest-mass density of a NS ($\rho_0 \lesssim 10^{15}$ g cm$^{-3}$) the GGL EOS is convex (blue regions), i.e., the fundamental derivatives $\mathcal{G}$ and $\mathcal{G}_R$ are both positive. By contrast, in the green region $\mathcal{G} \lesssim 0$ and so is the relativistic fundamental derivative. This is the nonconvex region of the EOS. There is also a

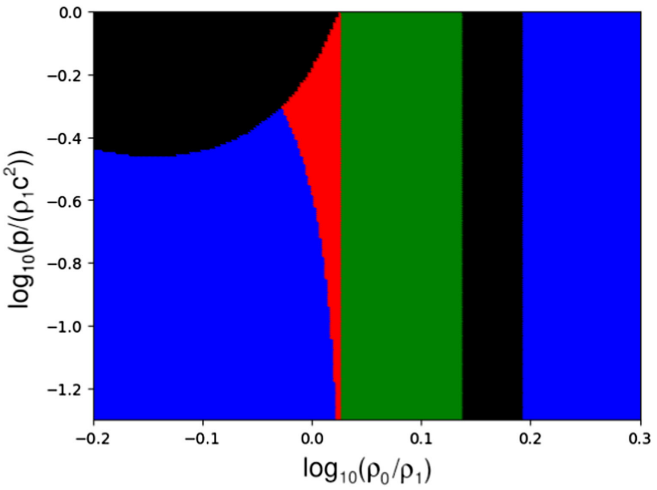


FIG. 3. Convexity behavior of the GGL EOS for the canonical values of the free parameters used in our simulations. We set $\Gamma_{\rm th} = 1.8$ (as in typical BNS simulations; see e.g., [14,88,89]), $\Gamma_1 = 3.0$, $\rho_1 = 9.1 \times 10^{14}$ g cm$^{-3}$, and $\Sigma = 0.35\rho_1$. The blue area corresponds to the region of the parameter space where the EOS is convex (i.e., $\mathcal{G} > 0$ and $\mathcal{G}_R > 0$). The green region corresponds to the region where $\mathcal{G} < 0$ (and thus $\mathcal{G}_R < 0$), i.e., the EOS is nonconvex. The red area is the relativistic nonconvex region (i.e., $\mathcal{G} > 0$ and $\mathcal{G}_R < 0$). Noncausal regions are displayed in black.

nonconvex relativistic region displayed in red where $\mathcal{G}_R < 0$, although $\mathcal{G} > 0$. Regions where the speed of sound becomes superluminal are shown in black. Our BNS simulations are tuned in such a way that their evolution takes place in the red and/or green regions.

## IV. RESULTS

We turn now to describe the results of our simulations. We first note that for every nonconvex model we consider (evolved with the GGL EOS), we also simulate the corresponding convex one, which is simply evolved using a constant value of the thermal index $\Gamma$ [simply achieved by setting $\Gamma_{\rm th} = \Gamma_1$ in Eq. (4)]. The main quantitative results of this comparison, with regard to the time of merger and to the GW peak frequency at merger, are reported in Table II.

### A. Morphology and dynamics

The binaries start from a coordinate separation of ∼44.3 km, which roughly corresponds to ∼6 orbits before merger. As GWs extract energy and angular momentum from the system, the coordinate orbital separation shrinks causing the stars to eventually merge forming a transient remnant with a lifetime $\gtrsim$15 ms.

During inspiral the dynamics for convex and nonconvex EOS is similar although some differences appear. In particular, we observe that a nonconvex dynamics tends to reduce the NS compactness compared to those with a convex dynamics. This behavior is somehow anticipated

TABLE II. Summary of key results. First three columns display the times and frequencies at merger reported in milliseconds, while the three last columns report the frequency in kiloHertz. Superindices denote the EOS used during the evolution: (i) const $\Gamma$ denotes $\Gamma = 1.8$; (ii) GGL, 3.0 denotes GGL with $\Gamma_{\rm th} = 1.8$ and $\Gamma_1 = 3.0$; and (iii) GGL, 3.5 denotes GGL with $\Gamma_{\rm th} = 1.8$ and $\Gamma_1 = 3.5$. We define the merger time as the peak GW amplitude. An empty cells denotes "not applicable."

| EOS | $t_{\rm mer}^{{\rm const}\,\Gamma}$ | $t_{\rm mer}^{\rm GGL,3.0}$ | $t_{\rm mer}^{\rm GGL,3.5}$ | $f_{\rm peak}^{{\rm const}\,\Gamma}$ | $f_{\rm peak}^{\rm GGL,3.0}$ | $f_{\rm peak}^{\rm GGL,3.5}$ |
|---|---|---|---|---|---|---|
| WFF1 | 19.70 | 9.00 | | 3.56 | 3.44 | |
| WFF2 | 18.79 | 10.43 | | 3.35 | 3.15 | |
| APR4 | 18.52 | 10.96 | 7.34 | 3.33 | 3.05 | 2.40 |
| SLy4 | 17.67 | 11.33 | 7.91 | 3.17 | 2.78 | 2.41 |
| APR3 | 17.33 | 11.50 | | 2.99 | 2.77 | |
| ENG | 17.14 | 11.43 | | 2.95 | 2.77 | |
| MPA1 | 16.31 | 11.97 | | 2.73 | 2.67 | |
| LS220 | 15.70 | 12.57 | 9.60 | 2.80 | 2.42 | 2.08 |
| ALF2 | 15.73 | 11.76 | | 2.70 | 2.52 | |
| DD2 | 14.66 | 12.39 | 9.67 | 2.57 | 2.29 | 2.09 |
| HShen | 12.47 | 12.06 | | 2.20 | 2.14 | |
| GNH3 | 13.78 | 12.96 | | 2.48 | 2.29 | |
| MS1 | 11.69 | 11.52 | | 2.18 | 2.04 | |

because during inspiral, the binary companion induces tidal forces that stretch the star out along the line connecting the centroids of the two stars. This effect triggers expansive shock waves in the bulk of a nonconvex NS pushing out its outer layers, which in turn accelerates the merger. We observe that this behavior depends on the EOS employed to build the initial data. The softer the EOS the shorter the merger time of the nonconvex binary compared with that of binaries with convex dynamics. Binaries built with soft EOS, such as WFF1 or APR4, when evolved with the GGL EOS merge $\gtrsim$5 ms earlier than their counterparts evolved with a constant $\Gamma = 1.8$ EOS. By contrast, binaries built with stiff EOS, such as DD2 or LS220, when evolved with the GGL EOS merge roughly at the same time ($\Delta t_{\rm mer} \lesssim 1$ ms) than their constant $\Gamma = 1.8$ EOS counterparts (see Table II). These different dynamics can also be deduced from Fig. 4 which displays the minimum value of the relativistic fundamental derivative $\mathcal{G}_R$ for binaries evolved with the GGL EOS and $\Gamma_1 = 3.0$. Soft EOS binaries tend to have smaller values of $\mathcal{G}_R$, and so are susceptible quite generally to developing strong expansive shock waves, that in turn puff the star out. By contrast, stiff EOS binaries tend to have larger values of $\mathcal{G}_R$, closer to zero, with expansive waves that only perturb the stars slightly. The dynamics of the latter mimics that of the convex binaries.

Following merger, a massive remnant forms with two dense cores rotating about each other. Depending on the compactness of the progenitors, and so on the value of the relativistic fundamental derivative (see Fig. 4), the two cores collide during the first $\lesssim$5 ms after merger giving

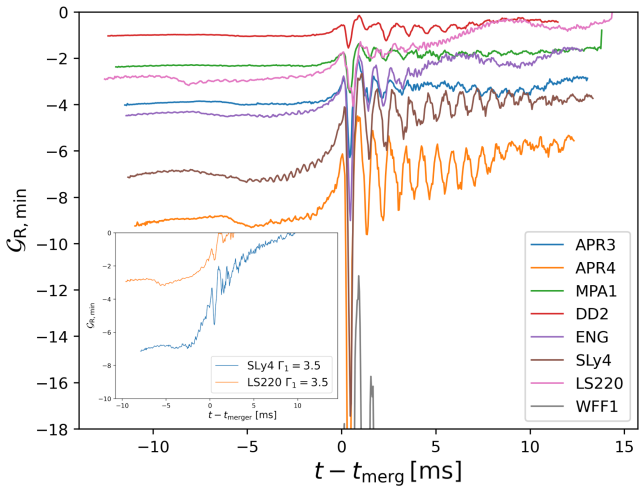


FIG. 4. Minimum value of the relativistic fundamental derivative $\mathcal{G}_R$ vs coordinate time for some selected EOSs, evolved with the GGL EOS setting $\Gamma_1 = 3.0$ (see Table II). The inset displays the evolution of $\mathcal{G}_R$ for two configurations evolved with $\Gamma_1 = 3.5$. Notice that the coordinate time has been shifted to the merger time.

birth to a highly differentially rotating star wrapped in a Keplearian-like cloud of low density matter. These rotational profiles are displayed in Fig. 5 at $t \sim 15$ ms after merger for some selected cases, but the behavior is similar

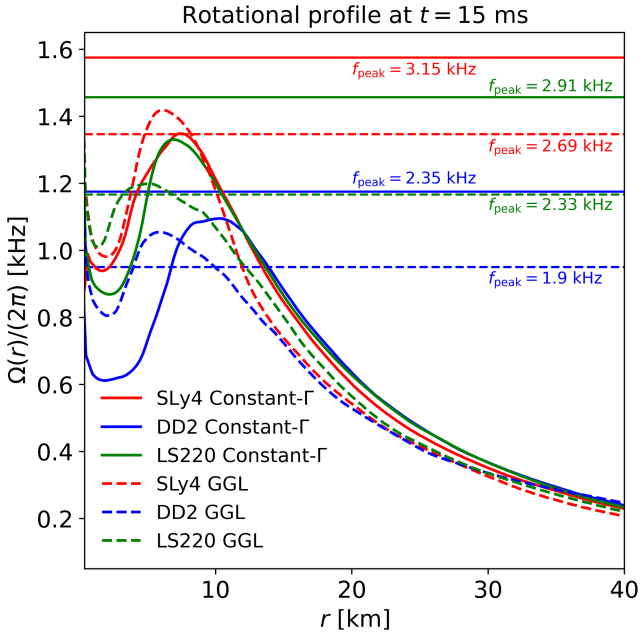


FIG. 5. Rotational profiles of the binary remnant along the coordinate radius $r$ at $t \sim 15$ ms after merger for the EOS indicated in the legend. Binaries with nonconvex (convex) dynamics are displayed with dashed (continuous) lines. Horizontal lines show the pattern speed frequencies of the main modes ($f_{\rm peak}/2$) for each model. The colors of the horizontal lines are the same as for the EOS labels. Similar profiles are observed for all other EOSs in Table I.

for all models we have evolved. At this stage of the evolution only the convex version of EOS SLy4 and LS220 are still in corotation with the pattern speed frequency of the dominant quadrupolar mode (shown by the horizontal lines). The remnant settles down shortly after that, i.e., the maximum value of the rest-mass density reaches a quasisteady state. In particular, we observe that the WFF1-GGL binary remnant settles down at $t_{\rm merg} \sim 5.5$ ms, the WFF1 remnant with $\Gamma = 1.8$ at $t_{\rm merg} \sim 4.2$ ms, while both the DD2-GGL and DD2 with $\Gamma = 1.8$ remnants settle down at about $t_{\rm merg} \sim 1.0$ ms.

Figure 6 displays the rest-mass density $\rho_0$ on the equatorial plane at $t \sim 6$ ms for some binary remnants in Table II (see legend at the bottom-left corner in each panel), normalized to its initial maximum value $\rho_{0,\max} \sim 10^{14.8}$ g cm$^{-3}$ (see Table I for all cases). The left half of each panel in this figure shows the snapshot of the evolution with the GGL EOS while the right half corresponds to the Γ-law EOS with $\Gamma = 1.8$. Following [11,90], we define the bulk of the remnant as the region enclosed by the rest-mass isodensity contour $\gtrsim 10^{12.5}$ g cm$^{-3}$. During the early post-merger evolution with the GGL EOS, the bulk of the remnant undergoes a transient period where nonconvex relativistic regions ($\mathcal{G}_R < 0$), identified by the green shaded areas in Fig. 6, expand and contract continuously. We observe that depending on the softness of the EOS these regions, as expected, may spread covering a large part of the bulk of the remnant or be confined around its central core. For all cases, once the remnant settles down we observe that the nonconvex regions remain bounded within $\rho_0 \gtrsim 10^{13.7}$ g cm$^{-3}$ (see Fig. 6). We note that, for all EOS listed in Table II, the remnants resulting from nonconvex evolutions are in general more extended than those of the convex ones, which implies that the presence of a nonconvex dynamics tends to increase the pressure support in the remnant. Therefore, one may conclude that nonconvex dynamics hardens the EOS of the remnant. Consistent with this, the angular velocity profiles shown in Fig. 5 for some of our models indicate that nonconvex remnants tend to rotate more rapidly at the core than convex ones. This behavior applies to our full set of models. Notice that this effect has also been observed in remnants undergoing quark-hadron phase transitions [16,28].

### B. Gravitational wave spectra

Figure 7 displays the GW spectra of the binaries for four representative initial-data EOS (APR4, DD2, LS220, and SLy4). The spectra are computed assuming a distance to the source of 50 Mpc, optimal orientation and sky localization, and using a fixed time window of 2 ms, from 20 ms before merger to 5 ms past merger. Following [14], we do not apply any windowing functions to obtain a cleaner separation of the contributions in the spectra. As a result, the FFT may include small artifacts due to the finite size of the

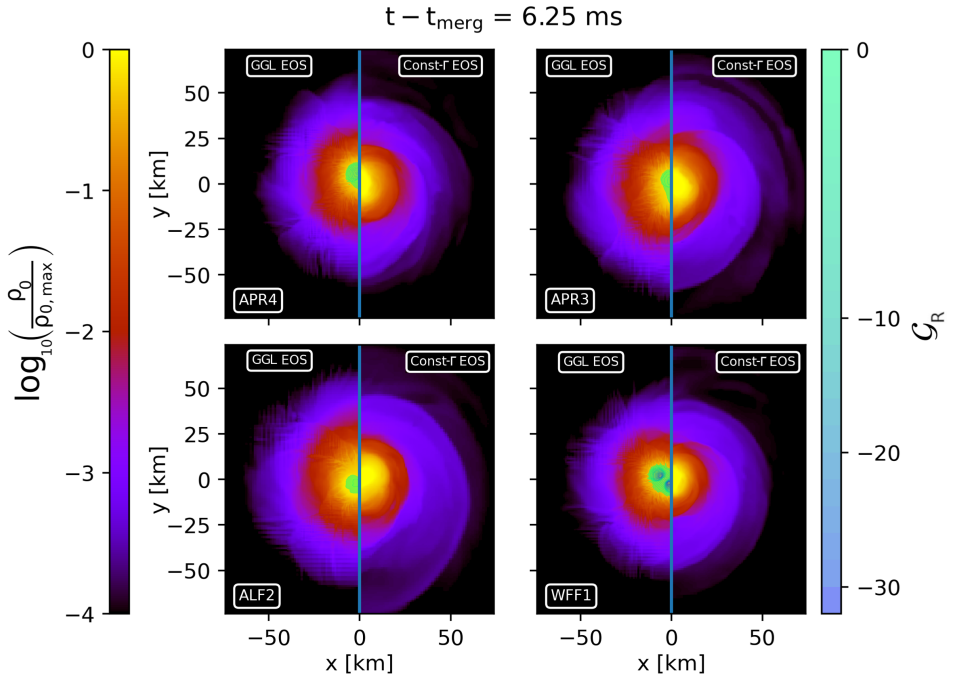


FIG. 6. Rest-mass density $\rho_0$, normalized to its initial maximum value $\rho_{0,\max} \sim 10^{14.8}$ g cm$^{-3}$ (see Table I for all cases), in log scale of the BNS remnant at $t \sim 6$ ms following merger for some of the EOSs listed in Table II. Negative values of the relativistic fundamental derivative are displayed in greenish (cold) color. Each panel shows a side-by-side comparison between the quasisteady configuration of the remnant evolved using either the phenomenological GGL EOS (left) or the constant Γ-law EOSs (right).

time intervals. Each panel in the figure contains three spectra, one obtained with a convex EOS and the other two with the nonconvex GGL EOS. To illustrate the impact of the free parameters of the GGL EOS, the last two spectra correspond to evolutions with $\Gamma_1 = 3.0$ and $\Gamma_1 = 3.5$. The frequencies of the dominant mode $f_{\rm peak}$ for each of these three evolutions are indicated with vertical dashed lines in each plot of the figure. The precise values are reported in the last three columns of Table II for all EOS.

During inspiral, the existence of $\mathcal{G}_R < 0$ regions slightly modifies the maximum GW frequency which reaches a maximum value below 2.2 KHz depending on the initial-data EOS. Following merger, the GW amplitude and frequency strongly depend on both the softness of the initial-data EOS and of the existence of nonconvex regions. Our simulations reveal that the frequency $f_{\rm peak}$ of the dominant oscillation mode of the remnant for binaries with nonconvex dynamics is always smaller than that of their convex dynamics counterparts (i.e., the peak frequency in nonconvex evolutions shifts to the left in Fig. 7). In the most extreme cases analyzed, a frequency shift of $\Delta f_{\rm peak} \sim 300$ Hz was found for the stiff DD2 EOS evolved with the GGL EOS with $\Gamma_1 = 3.0$ and a corresponding shift of $\Delta f_{\rm peak} \sim 1$ kHz was found for the soft APR4 EOS with $\Gamma_1 = 3.5$. All peak frequency values are reported in Table II for all cases.

It is well known that the GW spectra of the postmerger remnant strongly depend on the EOS (see e.g., [89,95,96]) and, in particular, it has been shown that the radius of the NS remnant depends on the peak prequency as $R_{\rm NS} \sim f_{\rm peak}^{-2/3}$ [97]. As the tidal deformability $\Lambda$ is basically a function of the chirp mass $\mathcal{M}$ and $R_{\rm NS}$ [98,99], it has been shown that future observations of the postmerger GW dominant mode could be used in combination with "quasiuniversal" relations between $\Lambda$ and $f_{\rm peak}$ (see e.g., [100,101]) to constraint the EOS of the NS. Notice that third-generation GW observatories may measure $f_{\rm peak}$ within an accuracy $\lesssim 30$ Hz [102–104]. Besides, it has also been suggested [21,29] that significant deviations of $f_{\rm peak}$ from these quasiuniversal relations with $\Lambda$ may indicate the presence of a first-order phase transition in the EOS leading to the formation of merger remnants with a quark-matter core. In particular [21,29] performed numerical studies of BNS mergers in which the stars were modeled with a hybrid DD2F-SF EOS that exhibits a strong first-order phase transition to deconfine quarks within the standard Maxwell approach [60,105]. Those simulations showed that there is a shift of up to $\Delta f_{\rm peak} \sim 700$ Hz with respect to the value of the frequency attained in BNS simulations modeled with the purely hadronic EOS DD2F, an EOS equivalent to DD2F-SF but without phase transitions.

The frequency shifts and "outliers" in the $f_{\rm peak} - \Lambda$ quasiuniversal relation found by [21,29] may be attributed to the existence of nonconvex dynamics in the postmerger remnant discussed here. Figure 8 displays the dominant

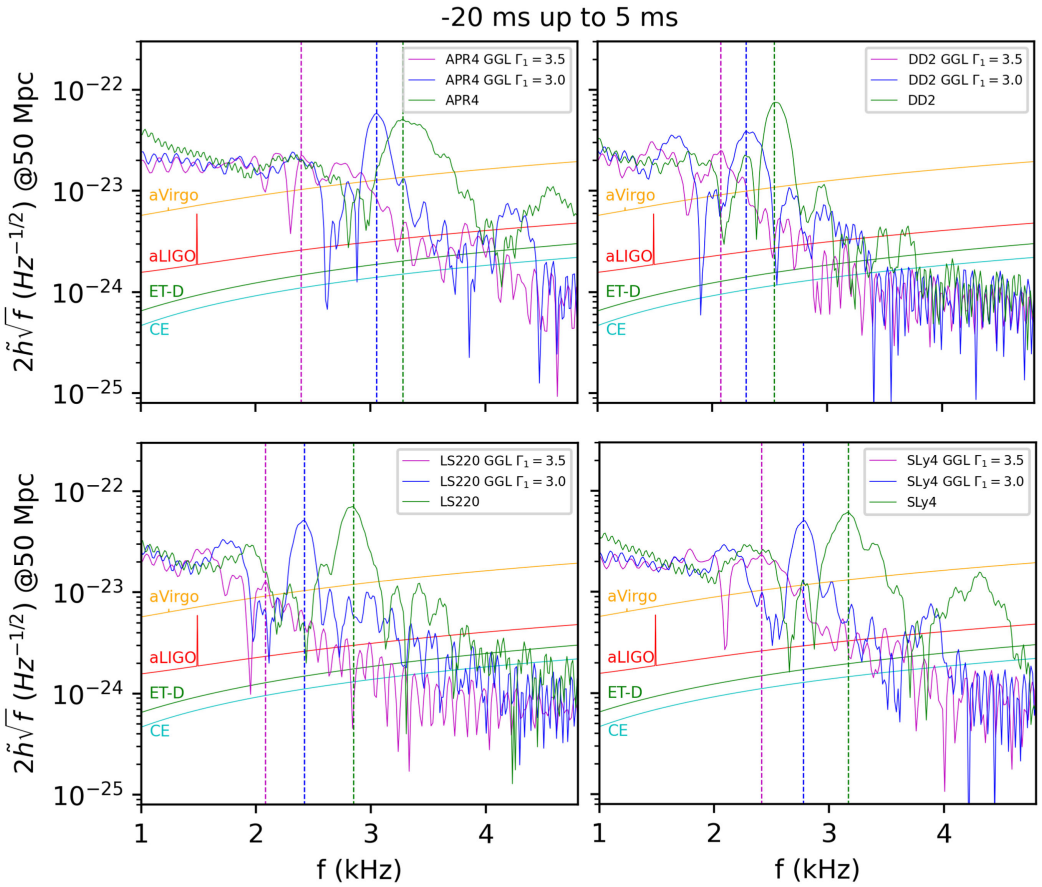


FIG. 7. GW spectra of both GGL and constant Γ-law binaries at 50 Mpc with optimal orientation and with a time window $t - t_{\rm mer} = [-20, 5]$ ms which emphasizes the contribution of the dominant spectral mode $f_{\rm peak}$ following merger. The two spectra for the GGL EOS correspond to $\Gamma_1 = 3.0$ and $\Gamma_1 = 3.5$. Sensitivity curves of Advanced Virgo (aVirgo) [91], Advanced LIGO (aLIGO) [92], Einstein Telescope (ET-D) [93], and Cosmic Explorer (CE) [94] are also displayed. Vertical lines mark the location of the peak frequency $f_{\rm peak}$.

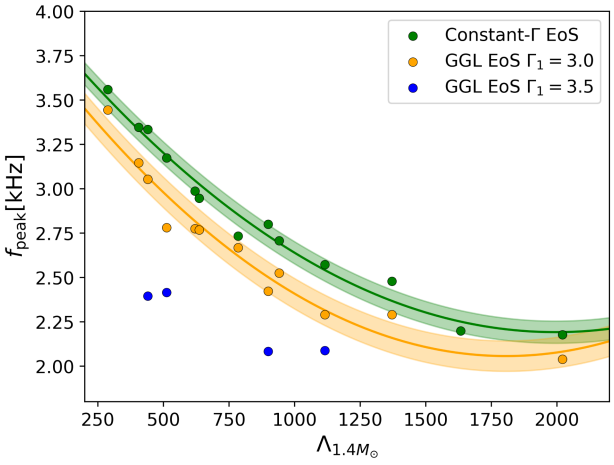


FIG. 8. GW peak frequency of the postmerger remnant $f_{\rm peak}$ as a function of the tidal deformability Λ for all simulations in Table II. Each circle corresponds to one initial-data EOS, the corresponding colors indicating the EOS used in the evolutions (see legend). Solid curves display the quasiuniversal relations given by Eqs. (8) and (9). Colored regions represent the standard deviation of the corresponding fit.

frequency as a function of the tidal deformability Λ for all evolutions listed in Table II. As expected, when the BNS merger is simulated using a convex EOS (green circles) $f_{\rm peak}$ is correlated with Λ in a quasiuniversal (EOS-insensitive) manner according to

$$f_{\rm peak}^{\rm const\,\Gamma} = [(4.52 \pm 0.79) \times 10^{-7}\Lambda^2 - (1.80 \pm 0.18) \times 10^{-3}\ \Lambda + (3.99 \pm 0.08)]\ \text{kHz}. \quad (8)$$

However, when the system is subject to nonconvex dynamics the peak frequency is more than 1–$\sigma$ away from the above quasiuniversal relation (yellow and blue circles in Fig. 8). We notice that a 1–$\sigma$ deviation in our previous fit corresponds to ∼64 Hz. This significant shift in frequency can solely be attributed in our study to the presence of a nonconvex dynamics and not to the presence of a physical process such as a phase transition in the binary remnant, as our GGL EOS does not account for such an effect, and neither to spurious artifacts induced by the numerical access to a tabulated EOS.

Notice that, in contrast with the results reported in [29] where the effects of the first-order phase transition increase the peak frequency of the dominant mode, the appearance of a nonconvex dynamics decreases this frequency. This discrepancy is simply due to the effective stiffening of the EOS remnant associated with our specific choice of the free parameters of our phenomenological GGL EOS, Eq. (4). However, the magnitude of the frequency shifts is, in both cases, comparable. We expect that a survey of parameters of the GGL EOS, in particular accounting for a softening of the EOS remnant, may not only reproduce the magnitude of the shifts but also reconcile the direction of the shift of the peak frequency with the values reported by [29].

Interestingly, we find that the outliers to the fitting formula (8) corresponding to binaries evolved with the GGL EOS setting $\Gamma_1 = 3.0$ satisfy their own quasiuniversal relation according to

$$f_{\rm peak}^{\rm GGL} = [(5.4 \pm 1.1) \times 10^{-7}\ \Lambda^2 - (1.95 \pm 0.25) \times 10^{-3}\ \Lambda + (3.82 \pm 0.12)]\ \text{kHz}, \tag{9}$$

with a deviation of $\Delta f_{\rm peak} \lesssim 380$ Hz with respect to binaries subject to convex dynamics. This finding suggests that the appearance of nonconvex regions might induce a displacement of the quasiuniversal relation on the $f_{\rm peak}$–$\Lambda$ plane for nonconvex EOSs.

The effects of a nonconvex dynamics on the postmerger GWs can be enhanced by fine-tuning the free parameters of the thermal index in Eq. (4). In particular, by setting $\rho_1 = 9.1 \times 10^{14}\ \text{g cm}^{-3}$, $\Sigma = 0.35\,\rho_1$, and $\Gamma_1 = 3.5$ we obtain the largest shift in $f_{\rm peak}$, namely $\sim$1 kHz (see Table II and the blue markers in Fig. 8).

To further corroborate that the frequency shifts observed in our nonconvex evolutions are due to the "anomalous" dynamics and not to the specific parameters of the GGL EOS of our fiducial model, we also simulate BNS mergers for the initial-data EOS DD2 with values of the GGL EOS parameters so that the evolution remains convex throughout (see the Appendix for details). In all cases we find that $10\ \text{Hz} \lesssim \Delta f_{\rm peak} \lesssim 50$ Hz, i.e., less than 1–$\sigma$ away from the quasiuniversal relation of Eq. (8) found for convex EOSs. This suggests that the significant shifts in the peak frequency reported in this paper should be induced by the nonconvex dynamics.

## V. DISCUSSION

Understanding the properties of matter beyond nuclear saturation density is essential for explaining GW observations of BNS mergers. Knowledge has been collected through combined experimental and theoretical efforts including EM and GW observations, nuclear physics experiments, and numerical simulations. The latter are distinctly driven by the ongoing GW observations of compact binary coalescences reported by the LIGO-Virgo-KAGRA (LVK) Collaboration [106] and by the expected significant increase in the rate of detections once third-generation detectors come online. Moreover, BNS mergers are the prime sources for multimessenger astronomy. EM, GW, and neutrino observations of these systems, in combination with theoretical and numerical work, will help advance our understanding of the origin of short gamma-ray bursts, $r$-process nucleosynthesis, or the nature of matter beyond nuclear saturation density.

In the past few years numerical simulations of BNS mergers have advanced in the treatment of the thermodynamics of the system, encoded in the EOS of high-density matter. Current simulations incorporate microphysical, finite-temperature EOS tables constructed using "tabulated" data from observations and nuclear physics experiments [16,29,73,88,107–110]. Some of the EOS employed also allow for phase transitions from nuclear hadronic matter into quark-gluon plasma or into matter phases containing exotic particles, processes that may modify the dynamics of the merger remnant and the GW emission. Numerical studies have searched for a first-order hadron-quark phase transition on the GWs (see e.g., [16,21,28–31]). In particular [21,29] reported a deviation of the quasiuniversal relation between the tidal deformability $\Lambda$ and the peak GW frequency at merger $f_{\rm peak}$ if the EOS allows for a strong first-order phase transition to deconfined quarks. The presence of a phase transition may also affect the monotonic increase of the speed of sound with density, turning a convex dynamics into a nonconvex one.

In this paper we have performed numerical-relativity simulations of BNS mergers subject to nonconvex dynamics, allowing for the appearance of expansive shock waves and compressive rarefactions. To this aim we have used a phenomenological nonconvex EOS proposed in [50] and also used in [51]. The latter work showed that the appearance of nonconvex dynamics during the gravitational collapse of uniformly rotating NS leaves a distinctive imprint on the GW signal, and served as a motivation for this study. Further motivation was gathered by our attempt to provide an explanation to the loss of the $\Lambda - f_{\rm peak}$ quasiuniversal relation found by [21,29] for EOS admitting a strong first-order phase transition. We have surveyed a number of BNS initial configurations modeled with a piecewise-polytropic representation of different (cold) nuclear EOS. Those have been subsequently evolved with a $\Gamma-$law EOS to allow for shock heating, considering two different possibilities for the adiabatic index $\Gamma$, either a constant value, which induces a convex (regular) dynamics, or a variable index depending on the rest-mass density, which induces a nonconvex (anomalous) dynamics.

By comparing the two types of dynamics—convex vs nonconvex—we have identified observable differences in

the GW spectra of the remnant. In particular, we have found that nonconvexity induces a significant shift in the $\Lambda - f_{\rm peak}$ quasiuniversal relation, of order $\Delta f_{\rm peak} \gtrsim 380\,{\rm Hz}$, with respect to that of binaries with convex dynamics. These values are similar in magnitude to those reported by [21,29], attributed however to a first-order phase transition from nuclear/hadronic matter to deconfined quark matter. We argue that the ultimate origin of the frequency shift is to be found in the presence of anomalous, nonconvex dynamics in the binary remnant.

The BNS merger simulations of [29] comprise an extensive number of EOS. Their fiducial model is based on the temperature-dependent, microscopic, hadron-quark hybrid EOS DD2F-SF of [111] and its nucleonic counterpart DD2F (with no phase transition). They consider different choices of parameters for the description of the quark phase, resulting in seven hybrid DD2F-SF EOS, which cover models with different onset densities and density jumps. In addition they also consider a representative sample of 15 EOSs describing purely hadronic models, three of which include a second-order phase transition to hyperonic matter, as well as the EOS ALF2 and EOS ALF4 from [61], which resemble models with a continuous transition to quark matter without a density jump. Out of all these EOS, the only ones departing from the tight quasiuniversal scaling between $f_{\rm peak}$ and the tidal deformability are the seven hybrid DD2F-SF EOS. For this subset of hybrid EOS [29] observed that the larger the density jump the more prominent the departure from the quasiuniversal relation. However, the three EOSs from their sample including a second-order phase transition to hyperonic matter were found to follow closely the $f_{\rm peak} - \Lambda$ relation similarly to a purely nucleonic EOS (in agreement with early results from [28]). The same scaling is found for EOS ALF2 and ALF4 in which the phase transition is continuous. In summary [29] conclude that only a sufficiently strong first-order phase transition can alter the postmerger GW signal in such a way that a measurable deviation from the $f_{\rm peak} - \Lambda$ relation occurs.

The fact that the scaling is lost only when the density jump is large enough might be, perhaps, an indication of possible numerical inaccuracies. In particular, the evaluation (through discretization) of high-order derivatives in tabulated dense-matter EOS across coexistence boundaries in phase transitions may introduce small-scale oscillations of numerical origin. This is visible in Fig. 1 (showing the results for the DD2F-SF EOS employed by [21,29]) and in Figs. 2 and 3 of [51]. We recall that those oscillations in the fundamental derivative are a numerical artifact due to the computation of the derivatives in $\mathcal{G}$ using a discrete EOS table. (See also [47] for an additional example of the numerical loss of convexity associated with insufficient thermodynamic discretization in tabulated EOS.) The effect of these oscillations is to spread spuriously the nonconvex behavior to points beyond the phase transition boundaries. In addition, as showed in [51], many of the microphysical EOSs investigated in that work display a sensitive reduction of the relativistic fundamental derivative as the baryon number density grows above 1 fm$^{-3}$. In that regime, even spurious small-scale oscillations may drive the relativistic fundamental derivative towards negative values. This would artificially trigger nonconvex thermodynamics of a numerical origin in those regions with number densities above 1 fm$^{-3}$. As suggested by [51], this artificial behavior could be attenuated using a finer number of data points in those regions of the EOS tables where the fundamental derivative displays large variations (i.e., near the boundaries of first-order phase transitions), specially if these variations drive $\mathcal{G}$ to negative values.

The phenomenological GGL EOS employed in the simulations reported in this work can only be regarded as a toy model. Nevertheless, it has served the purpose of highlighting the potential relevance the development of nonconvex dynamics may have on important observables in BNS mergers such as the GW emission (as was also shown by [51] in the context of gravitational collapse). Notice that the free parameters of our EOS have been chosen such that the dynamics of the binary is always nonconvex. In particular, for all our simulations $\Gamma_1 > \Gamma_{\rm th}$ which induces a stiffer EOS compared to the constant $\Gamma$-law EOS (convex models). One might also consider a softer GGL EOS by choosing $\Gamma_1 < \Gamma_{\rm th}$ and analyze the impact of the EOS stiffness on the nonconvex dynamics. Such a study has not been attempted in this work. We hypothesize that our results are robust against changes in the stiffness of the phenomenological GGL EOS as long as the resulting dynamics is nonconvex, since the latest is responsible for hardening the EOS of the binary remnant. We stress that our GGL EOS does not account for phase transitions and is not affected by potential spurious artifacts induced by the numerical access to a tabulated EOS as all derivatives can be computed analytically. A natural extension of this work will be to revisit these simulations using actual microphysical EOS allowing for such nonconvex dynamics. Those could also be carried out in combination with the analytic model for modeling phase transitions in tabulated EOSs recently reported by [54].

## ACKNOWLEDGMENTS

We thank José María Ibáñez for a careful reading of the manuscript and for providing insightful comments. Work supported by the Generalitat Valenciana (Grants No. CIDEGENT/2021/046 and No. Prometeo CIPROM/2022/49), and by the Spanish Agencia Estatal de Investigación (Grants No. PID2021-125485NB-C21 funded by MCIN/AEI/10.13039/501100011033, No. PRE2019-087617, and ERDF A way of making Europe). Further support has been provided by the EU's Horizon 2020 Research and Innovation (RISE) programme H2020-MSCA-RISE-2017 (FunFiCO-777740) and by the EU

Staff Exchange (SE) programme HORIZON-MSCA-2021-SE-01 (NewFunFiCO-101086251). We acknowledge computational resources and technical support of the Spanish Supercomputing Network through the use of MareNostrum at the Barcelona Supercomputing Center (AECT-2023-1-0006). This work has used the following open-source packages: NumPy [112], SciPy [113], SCIKIT-LEARN [114], and Matplotlib [115]. Finally, we thank the authors of [14] for making available the PyCactus Python post-process package for analyzing output of Eistein Toolkit.

## APPENDIX: IMPACT OF Γ ON $f_{\rm peak}$

Thermal effects to account for shock heating during merger are modeled in our simulations using a hybrid approach, in which the EOS has a cold part and a thermal part [see Eq. (5)]. The value of the thermal index Γ appearing in the ideal-gaslike part of the pressure can be chosen somewhat arbitrarily, as long as it lays in the range $1 \leq \Gamma \leq 2$ due to causality constraints (see e.g., [89]). However, the choice of Γ controls the thermal pressure produced during and after merger [see Eq. (6)]. In this appendix we address if the observed shift on $f_{\rm peak}$ could be triggered by changes in the value of Γ. To do so we evolve the BNS built with the initial-data DD2 EOS using both the constant Γ-law and the GGL EOS using the parameters in Table III. We tune these parameters such that the dynamics of the system remains convex during the whole evolution. In all cases we find that the shift in the frequency of the dominant mode is $\Delta f_{\rm peak} \lesssim 50$ Hz (see last column in Table III). These results imply that the changes on the GW spectra discussed in this work are triggered by the non-convex dynamics of the BNS mergers.

TABLE III. Summary of the parameters of the GGL EOS used to evolve a BNS built with the initial-data DD2 EOS. The choice of parameters guarantees a convex dynamics in all cases. The last column reports the shift on the peak frequency with respect to our fiducial $\Gamma_{\rm th} = 1.8$, $\Gamma_1 = 3.0$ case. Here $\rho_0$ denotes the initial value of the central density $\rho_0 = 5.70 \times 10^{14}$ g cm$^{-3}$. An empty cells denotes "not applicable."

| $\Gamma_{\rm th}$ | $\Gamma_1$ | $\Sigma$ | $\rho_1/\rho_0$ | $\Delta f_{\rm peak}$ [Hz] |
|---|---|---|---|---|
| 1.36 | 1.36 | | | 13 |
| 1.8 | 1.36 | $0.3\rho_1$ | 0.69 | 26 |
| 1.8 | 2.0 | $0.35\rho_1$ | 0.91 | 53 |
| 2.0 | 2.0 | | | 40 |

[1] F. Zappa, S. Bernuzzi, D. Radice, A. Perego, and T. Dietrich, Phys. Rev. Lett. **120**, 111101 (2018).
[2] M. Maggiore *et al.*, J. Cosmol. Astropart. Phys. 03 (2020) 050.
[3] M. Branchesi *et al.*, J. Cosmol. Astropart. Phys. 07 (2023) 068.
[4] M. Evans *et al.*, arXiv:2109.09882.
[5] A. Bauswein and N. Stergioulas, J. Phys. G **46**, 113002 (2019).
[6] N. K. Glendenning, *Compact stars: Nuclear physics, particle physics, and general relativity* (Springer, New York, 1997).
[7] H. Heiselberg and M. Hjorth-Jensen, Phys. Rep. **328**, 237 (2000).
[8] P. Haensel, A. Y. Potekhin, and D. G. Yakovlev, *Neutron Stars 1: Equation of State and Structure* (Springer, New York, USA, 2007), Vol. 326.
[9] T. Soultanis, A. Bauswein, and N. Stergioulas, Phys. Rev. D **105**, 043020 (2022).
[10] K. Topolski, S. Tootle, and L. Rezzolla, arXiv:2310.10728.
[11] W. Kastaun, R. Ciolfi, and B. Giacomazzo, Phys. Rev. D **94**, 044060 (2016).
[12] M. Hanauske, K. Takami, L. Bovard, L. Rezzolla, J. A. Font, F. Galeazzi, and H. Stöcker, Phys. Rev. D **96**, 043004 (2017).
[13] C. A. Raithel and V. Paschalidis, Phys. Rev. D **108**, 083029 (2023).
[14] R. De Pietri, A. Feo, J. A. Font, F. Löffler, M. Pasquali, and N. Stergioulas, Phys. Rev. D **101**, 064052 (2020).
[15] M. G. Orsaria, G. Malfatti, M. Mariani, I. F. Ranea-Sandoval, F. García, W. M. Spinella, G. A. Contrera, G. Lugones, and F. Weber, J. Phys. G **46**, 073002 (2019).
[16] E. R. Most, L. J. Papenfort, V. Dexheimer, M. Hanauske, S. Schramm, H. Stöcker, and L. Rezzolla, Phys. Rev. Lett. **122**, 061101 (2019).
[17] N. Chamel, A. F. Fantina, J. M. Pearson, and S. Goriely, Astron. Astrophys. **553**, A22 (2013).
[18] H. Kochankovski, A. Ramos, and L. Tolos, Mon. Not. R. Astron. Soc. **517**, 507 (2022).
[19] A. R. Raduta, F. Nacu, and M. Oertel, Eur. Phys. J. A **57**, 329 (2021).
[20] A. R. Raduta, Eur. Phys. J. A **58**, 115 (2022).
[21] S. Blacker, N.-U. F. Bastian, A. Bauswein, D. B. Blaschke, T. Fischer, M. Oertel, T. Soultanis, and S. Typel, Phys. Rev. D **102**, 123023 (2020).
[22] A. Bazavov *et al.*, Phys. Rev. Lett. **109**, 192302 (2012).
[23] S. Borsanyi, Z. Fodor, C. Hoelbling, S. D. Katz, S. Krieg, and K. K. Szabo, Phys. Lett. B **730**, 99 (2014).
[24] A. Bazavov *et al.* (HotQCD Collaboration), Phys. Rev. D **90**, 094503 (2014).
[25] T. Krüger, I. Tews, K. Hebeler, and A. Schwenk, Phys. Rev. C **88**, 025802 (2013).
[26] A. Kurkela, E. S. Fraga, J. Schaffner-Bielich, and A. Vuorinen, Astrophys. J. **789**, 127 (2014).
[27] A. Lovato *et al.*, arXiv:2211.02224.
[28] D. Radice, S. Bernuzzi, W. Del Pozzo, L. F. Roberts, and C. D. Ott, Astrophys. J. Lett. **842**, L10 (2017).

[29] A. Bauswein, N.-U. F. Bastian, D. B. Blaschke, K. Chatziioannou, J. A. Clark, T. Fischer, and M. Oertel, Phys. Rev. Lett. **122**, 061102 (2019).
[30] S. L. Liebling, C. Palenzuela, and L. Lehner, Classical Quantum Gravity **38**, 115007 (2021).
[31] M. Ujevic, H. Gieg, F. Schianchi, S. V. Chaurasia, I. Tews, and T. Dietrich, Phys. Rev. D **107**, 024025 (2023).
[32] S. Fujibayashi, Y. Sekiguchi, K. Kiuchi, and M. Shibata, Astrophys. J. **846**, 114 (2017).
[33] P. Bedaque and A. W. Steiner, Phys. Rev. Lett. **114**, 031103 (2015).
[34] L. McLerran and S. Reddy, Phys. Rev. Lett. **122**, 122701 (2019).
[35] H. Tan, T. Dore, V. Dexheimer, J. Noronha-Hostler, and N. Yunes, Phys. Rev. D **105**, 023018 (2022).
[36] R. Somasundaram, I. Tews, and J. Margueron, Phys. Rev. C **107**, 025801 (2023).
[37] N. Yao, A. Sorensen, V. Dexheimer, and J. Noronha-Hostler, arXiv:2311.18819.
[38] D. Mroczek, M. C. Miller, J. Noronha-Hostler, and N. Yunes, arXiv:2309.02345.
[39] D. Dey, J. Amrit Pattnaik, H. C. Das, A. Kumar, R. N. Panda, and S. K. Patra, arXiv:2401.02190.
[40] P. Haensel and A. Y. Potekhin, Astron. Astrophys. **428**, 191 (2004).
[41] R. Menikoff and B. J. Plohr, Rev. Mod. Phys. **61**, 75 (1989).
[42] E. F. Toro, *Riemann Solvers and Numerical Methods for Fluid Dynamics* (Springer, Berlin, Heidelberg, 2009).
[43] P. A. Thompson, Phys. Fluids **14**, 1843 (1971).
[44] S. Typel, M. Oertel, and T. Klähn, Phys. Part. Nucl. **46**, 633 (2015).
[45] M. Oertel, M. Hempel, T. Klähn, and S. Typel, Rev. Mod. Phys. **89**, 015007 (2017).
[46] https://stellarcollapse.org/SROEOS.
[47] B. Vaidya, A. Mignone, G. Bodo, and S. Massaglia, Astron. Astrophys. **580**, A110 (2015).
[48] J. M. Ibáñez, I. Cordero-Carrión, J. M. Martí, and J. A. Miralles, Classical Quantum Gravity **30**, 057002 (2013).
[49] J.-M. Ibáñez, I. Cordero-Carrión, M.-Á. Aloy, J.-M. Martí, and J.-A. Miralles, Classical Quantum Gravity **32**, 095007 (2015).
[50] J. M. Ibáñez, A. Marquina, S. Serna, and M. A. Aloy, Mon. Not. R. Astron. Soc. **476**, 1100 (2018).
[51] M. A. Aloy, J. M. Ibáñez, N. Sanchis-Gual, M. Obergaulinger, J. A. Font, S. Serna, and A. Marquina, Mon. Not. R. Astron. Soc. **484**, 4980 (2019).
[52] A. Marquina, S. Serna, and J. M. Ibáñez, J. Sci. Comput. **81**, 2132 (2019).
[53] M. Berbel and S. Serna, Phys. Rev. D **108**, 083031 (2023).
[54] M. Berbel, S. Serna, and A. Marquina, J. Fluid Mech. **975**, A48 (2023).
[55] Y. Lim and J. W. Holt, arXiv:1909.09089.
[56] H. A. Bethe, On the theory of shock waves for an arbitrary equation of state, in *Classic Papers in Shock Compression Science*, edited by J. N. Johnson and R. Chéret (Springer, New York, NY, 1998), pp. 421–495.
[57] Y. B. Zel'Dovich, Zh. Eksp. Teor. Fiz. **4**, 337 (1946).
[58] P. Cinnella and P. M. Congedo, J. Fluid Mech. **580**, 179 (2007).
[59] P. Cinnella, P. M. Congedo, V. Pediroda, and L. Parussini, Phys. Fluids **23**, 116101 (2011).
[60] https://compose.obspm.fr/home.
[61] J. S. Read, B. D. Lackey, B. J. Owen, and J. L. Friedman, Phys. Rev. D **79**, 124032 (2009).
[62] E. Gourgoulhon, P. Grandclement, K. Taniguchi, J.-A. Marck, and S. Bonazzola, Phys. Rev. D **63**, 064029 (2001).
[63] K. Taniguchi and E. Gourgoulhon, Phys. Rev. D **66**, 104019 (2002).
[64] http://www.lorene.obspm.fr/.
[65] T. E. Riley *et al.*, Astrophys. J. Lett. **918**, L27 (2021).
[66] E. Fonseca *et al.*, Astrophys. J. **832**, 167 (2016).
[67] J. Antoniadis *et al.*, Science **340**, 6131 (2013).
[68] H. T. Cromartie *et al.* (NANOGrav Collaboration), Nat. Astron. **4**, 72 (2019).
[69] B. P. Abbott *et al.* (LIGO Scientific and Virgo Collaborations), Phys. Rev. Lett. **121**, 161101 (2018).
[70] R. Abbott, T. D. Abbott, and S. Abraham (LIGO Scientific and Virgo Collaborations), Astrophys. J. Lett. **896**, L44 (2020).
[71] T. E. Riley *et al.*, Astrophys. J. Lett. **887**, L21 (2019).
[72] B. P. Abbott *et al.* (LIGO Scientific and Virgo Collaborations), Phys. Rev. Lett. **119**, 161101 (2017).
[73] L. R. Werneck *et al.*, Phys. Rev. D **107**, 044037 (2023).
[74] Z. B. Etienne, V. Paschalidis, R. Haas, P. Mösta, and S. L. Shapiro, Classical Quantum Gravity **32**, 175009 (2015).
[75] F. Loffler, J. Faber, E. Bentivegna, T. Bode, P. Diener *et al.*, Classical Quantum Gravity **29**, 115001 (2012).
[76] E. Schnetter, S. H. Hawley, and I. Hawke, Classical Quantum Gravity **21**, 1465 (2004).
[77] T. W. Baumgarte and S. L. Shapiro, Phys. Rev. D **59**, 024007 (1999).
[78] M. Shibata and T. Nakamura, Phys. Rev. D **52**, 5428 (1995).
[79] H. O. Kreiss and J. Lorenz, *Initial-Boundary Value Problems and the Navier-Stokes Equations* (Academic Press, San Diego, 1989).
[80] L. Antón, O. Zanotti, J. A. Miralles, J. M. Martí, J. M. Ibáñez, J. A. Font, and J. A. Pons, Astrophys. J. **637**, 296 (2006).
[81] F. Banyuls, J. A. Font, J. M. Ibáñez, J. M. Martí, and J. A. Miralles, Astrophys. J. **476**, 221 (1997).
[82] J. A. Font, Living Rev. Relativity **11**, 7 (2008).
[83] P. Colella and P. R. Woodward, J. Comput. Phys. **54**, 174 (1984).
[84] A. Harten, P. D. Lax, and B. v. Leer, SIAM Rev. **25**, 35 (1983).
[85] B. M. Argrow, Shock Waves **6**, 241 (1996).
[86] A. Guardone and L. Vigevano, J. Comput. Phys. **175**, 50 (2002).
[87] S. Serna and A. Marquina, Phys. Fluids **26**, 016101 (2014).
[88] D. Guerra *et al.* (to be published).
[89] K. Takami, L. Rezzolla, and L. Baiotti, Phys. Rev. D **91**, 064001 (2015).
[90] M. Ruiz, A. Tsokaros, and S. L. Shapiro, Phys. Rev. D **104**, 124049 (2021).
[91] F. e. a. Acernese (Virgo Collaboration), Classical Quantum Gravity **32**, 024001 (2015).
[92] LIGO Scientific Collaboration, Free software (GPL), 10.7935/GT1W-FZ16 (2018).

[93] S. e. a. Hild (ET Collaboration), Classical Quantum Gravity **28**, 094013 (2011).
[94] B. P. Abbott *et al.* (LIGO Scientific Collaboration), Classical Quantum Gravity **34**, 044001 (2017).
[95] A. Bauswein and N. Stergioulas, Phys. Rev. D **91**, 124056 (2015).
[96] S. Vretinaris, N. Stergioulas, and A. Bauswein, Phys. Rev. D **101**, 084039 (2020).
[97] A. Bauswein and H. T. Janka, Phys. Rev. Lett. **108**, 011101 (2012).
[98] S. De, D. Finstad, J. M. Lattimer, D. A. Brown, E. Berger, and C. M. Biwer, Phys. Rev. Lett. **121**, 091102 (2018); **121**, 259902(E) (2018).
[99] S. Bose, K. Chakravarti, L. Rezzolla, B. S. Sathyaprakash, and K. Takami, Phys. Rev. Lett. **120**, 031102 (2018).
[100] L. Rezzolla and K. Takami, Phys. Rev. D **93**, 124051 (2016).
[101] K. Topolski, S. Tootle, and L. Rezzolla, Astrophys. J. **960**, 86 (2024).
[102] J. Clark, A. Bauswein, L. Cadonati, H. T. Janka, C. Pankow, and N. Stergioulas, Phys. Rev. D **90**, 062004 (2014).
[103] H. Yang, V. Paschalidis, K. Yagi, L. Lehner, F. Pretorius, and N. Yunes, Phys. Rev. D **97**, 024049 (2018).
[104] A. Torres-Rivas, K. Chatziioannou, A. Bauswein, and J. A. Clark, Phys. Rev. D **99**, 044014 (2019).
[105] S. Typel, G. Ropke, T. Klahn, D. Blaschke, and H. H. Wolter, Phys. Rev. C **81**, 015803 (2010).
[106] R. Abbott *et al.* (KAGRA, Virgo, and LIGO Scientific Collaborations), Phys. Rev. X **13**, 041039 (2023).
[107] R. Oechslin, H. T. Janka, and A. Marek, Astron. Astrophys. **467**, 395 (2007).
[108] A. Bauswein, H. T. Janka, and R. Oechslin, Phys. Rev. D **82**, 084043 (2010).
[109] Y. Sekiguchi, K. Kiuchi, K. Kyutoku, and M. Shibata, Phys. Rev. Lett. **107**, 051102 (2011).
[110] P. L. Espino, G. Bozzola, and V. Paschalidis, Phys. Rev. D **107**, 104059 (2023).
[111] T. Fischer, N.-U. F. Bastian, M.-R. Wu, P. Baklanov, E. Sorokina, S. Blinnikov, S. Typel, T. Klähn, and D. B. Blaschke, Nat. Astron. **2**, 980 (2018).
[112] C. R. Harris *et al.*, Nature (London) **585**, 357 (2020).
[113] P. Virtanen *et al.* (SciPy 1.0 Contributors), Nat. Methods **17**, 261 (2020).
[114] F. Pedregosa, G. Varoquaux, A. Gramfort, V. Michel, B. Thirion, O. Grisel, M. Blondel, P. Prettenhofer, R. Weiss, V. Dubourg, J. Vanderplas, A. Passos, D. Cournapeau, M. Brucher, M. Perrot, and E. Duchesnay, J. Mach. Learn. Res. **12**, 2825 (2011).
[115] J. D. Hunter, Comput. Sci. Eng. **9**, 90 (2007).